CrossMark

Simulating the Formation and Eruption of Flux Rope by Magneto-friction Model Driven by Time-dependent Electric Fields

P. Vemareddy⬚

Indian Institute of Astrophysics, II Block, Koramangala, Bengaluru-560 034, India

Abstract

Aiming to capture the formation and eruption of flux ropes (FRs) in the source active regions (ARs), we simulate the coronal magnetic field evolution of the AR 11429 employing the time-dependent magneto-friction model (TMF). The initial field is driven by electric fields that are derived from time-sequence photospheric vector magnetic field observations by invoking ad hoc assumptions. The simulated magnetic structure evolves from potential to twisted fields over the course of two days, followed by rise motion in the later evolution, depicting the formation of an FR and its slow eruption later. The magnetic configuration resembles an inverse S-sigmoidal structure, composed of the potential field enveloping the inverse J-shaped fields that are sheared past one another and a low-lying twisted field along the major polarity inversion line. To compare with observations, proxy emission maps based on averaged current density along the field lines are generated from the simulated field. These emission maps exhibit a remarkable one-to-one correspondence with the spatial characteristics in coronal extreme ultraviolet images, especially the filament trace supported by the twisted magnetic field in the southwest subregion. Further, the topological analysis of the simulated field reveals the cospatial flare ribbons with the quasi-separatrix layers, which is consistent with the standard flare models; therefore, the extent of the twist and orientation of the erupting FR is indicated to be the real scenario in this case. The TMF model simulates the coronal field evolution, correctly capturing the formation of the FR in the observed timescale and the twisted field generated from these simulations serves as the initial condition for the full MHD simulations.

Unified Astronomy Thesaurus concepts: Solar coronal mass ejections (310); Solar magnetic fields (1503); Solar active regions (1974); Magnetohydrodynamical simulations (1966)

Materials only available in the online version of record: animations

1. Introduction

Coronal mass ejections and flares are the most spectacular and dangerous manifestations of solar activity. They are believed to be powered by the release of vast amounts of magnetic energy (T. Wiegelmann et al. 2017). These events occur from the corona of the active regions (ARs) where intense magnetic fields are present. Coronal imaging observations in extreme ultraviolet (EUV) and soft X-ray wave bands reveal that the corona has a complex and evolving magnetic structure that is continuously driven by ubiquitous plasma motions at the photospheric surface. Because the solar corona satisfies the low-β plasma condition, magnetic fields play a fundamental role in these energetic events (K. Shibata & T. Magara 2011), and therefore understanding the structure and evolution of the coronal magnetic fields is crucial to comprehending the genesis of the space weather affecting solar events.

High-resolution and high-cadence magnetic field measurements of the photospheric surface are regularly available from the ground (e.g., J. W. Harvey et al. 1996; C. U. Keller et al. 2003) and space (e.g., P. H. Scherrer et al. 1995, 2012) instruments, but the coronal magnetic field measurements are difficult to make due to tenuous plasma conditions. There are occasionally direct measurements of the coronal field available off the solar limb (e.g., H. Lin et al. 2004; S. Tomczyk et al.

2008; E. Landi et al. 2020; R. Si et al. 2020). However, these measurements frequently suffer from line-of-sight confusion and inadequate spatial or temporal resolution, making accurate interpretation difficult. While coronal magnetometry is still being developed (S. E. Gibson et al. 2016; N. E. Raouafi et al. 2016), significant research has been focused on numerical modeling of the coronal magnetic field using photospheric vector magnetograms (e.g., G. A. Gary 1989; T. Sakurai 1989; C. J. Schrijver et al. 2008) in the past two decades.

Nonlinear force-free field (NLFFF) models have been used to reconstruct the three-dimensional (3D) coronal magnetic field using the observed photospheric magnetograms (e.g., M. L. DeRosa et al. 2009; S. Régnier 2013; T. Wiegelmann et al. 2017). These models' main assumption is that the Lorentz force vanishes in the corona, allowing field-aligned currents to deform the field geometry, thereby offering estimates of magnetic non-potential quantities such as relative magnetic helicity and free magnetic energy. The NLFFF models have been employed to study the coronal magnetic structure constituting topological features such as null points, twisted flux tubes, and flux ropes (FRs; e.g., S. Régnier & T. Amari 2004; S. Masson et al. 2009; P. Vemareddy & T. Wiegelmann 2014; P. Vemareddy & P. Demoulin 2018). The extrapolated magnetic structure is validated by comparing the chosen model field lines with the observed magnetic structure in, e.g., EUV or soft X-ray images. These models are successful in yielding comparable structures resembling the observed ones in most of the cases (C. J. Schrijver et al. 2008; M. L. DeRosa et al. 2009). It is important to note that the extrapolated magnetic fields represent static fields in

equilibrium where the dynamic evolution is missing. A useful technique for producing the dynamical evolution of the magnetic fields in the AR corona is to use magnetohydro-dynamic (MHD) simulations (e.g., Z. Mikić et al. 1999; S. Inoue 2016; S. Toriumi et al. 2020; C. Jiang et al. 2022). These simulations involve advancing the full MHD equations in time and are physically realistic to capture information about plasma flow, density, and temperature in addition to the magnetic field (e.g., Z. Mikić et al. 1999; B. V. Gudiksen & Å. Nordlund 2002) during various physical processes such as flare reconnection in the computational domain. Even though these full MHD simulations are physically realistic, they are computationally expensive for domains of the AR size at meaningful resolutions, particularly when examining long-term evolution on the order of a few days.

The magneto-friction (MF; W. H. Yang et al. 1986) method is another approach to construct NLFFF based on the induction equation alone (e.g., G. Valori et al. 2005; M. G. Bobra et al. 2008). In this approach, the inductive velocity is proportional to the Lorentz force, which is relaxed to a force-free state over time. The MF model can be driven by the time series of lower boundary observations to simulate the dynamical evolution of the coronal magnetic field (A. A. van Ballegooijen et al. 2000; D. H. Mackay et al. 2011). In the wake of the availability of time-series photospheric magnetic field observations at high cadence and high resolution from the Helioseismic and Magnetic Imager (HMI; J. Schou et al. 2012) on board Solar Dynamics Observatory (SDO), time-dependent data-driven MF simulations have become a useful technique to study the long-term evolution of the ARs.

Utilizing the line-of-sight component of magnetic fields, inductive components of electric fields are derived by inversion methods developed by G. H. Fisher et al. (2010). The inductive electric fields have been used to drive the coronal field (D. H. Mackay et al. 2011; G. P. S. Gibb et al. 2014). In these simulations, the energy injection depends on the line-of-sight (LOS) component alone, and the information of the horizontal magnetic field is missing to supply enough energy input into the coronal field. To account for additional energy injection, M. C. M. Cheung & M. L. DeRosa (2012) supplemented the non-inductive components to the inductive ones by employing ad hoc assumptions and found that the non-inductive electric fields are crucial for significant energy injection that is essential to form energized magnetic structures such as FRs in the corona. Further, such simulations have been employed to study the formation of the helical jets and twisted FRs in the ARs over days (M. C. M. Cheung et al. 2015; J. Pomoell et al. 2019). In this article, using the time-dependent MF model, we simulate the coronal field evolution in AR 11429 by driving the initial field with electric fields that are derived from a time sequence of observed vector magnetic fields. The numerical setup and methodology are described in Section 2. A detailed analysis of the simulated magnetic fields in comparison with coronal observations is presented in Section 3, and a summary of the results is outlined in Section 4.

2. Simulation Model and Setup

2.1. Coronal Field Model

We simulate the coronal magnetic field evolution by the MF method (W. H. Yang et al. 1986), where the magnetic field evolves in response to the photospheric flux motions through the non-ideal induction equation given by

$$\frac{\partial \boldsymbol{A}}{\partial t} = \boldsymbol{v}_{\mathrm{MF}} \times \boldsymbol{B} - \eta \mu_0 \boldsymbol{J} \tag{1}$$

where $\boldsymbol{v}_{\mathrm{MF}}$ is the magnetic frictional plasma velocity, and $\boldsymbol{A}$ is the vector potential relating the magnetic field as $\boldsymbol{B} = \nabla \times \boldsymbol{A}$. The second term is to accommodate dissipation in the corona due to electric currents $\boldsymbol{J} = \nabla \times \boldsymbol{B}/\mu_0$. The magnetic diffusiv-ity can be chosen as a typical value of $\eta = 1 \times 10^8 \,\mathrm{m^2\,s^{-1}}$ to be able to run the simulation stably. Here, the induction equation is solved in terms of $\boldsymbol{A}$ to ensure that $\nabla \cdot \boldsymbol{B} = 0$ without additional divergence-free schemes. From the assumption of static magnetic fields, the MF velocity is given by

$$\boldsymbol{v}_{\mathrm{MF}} = \frac{1}{\nu} \frac{\mu_0 \, \boldsymbol{J} \times \boldsymbol{B}}{B^2} \tag{2}$$

where ν is the magneto-frictional coefficient that controls the speed of the relaxation process and μ_0 is the magnetic permeability in vacuum. As suggested in M. C. M. Cheung & M. L. DeRosa (2012), a height-dependent form of the frictional coefficient ν is given by

$$\frac{1}{\nu} = \frac{1}{\nu_0}(1 - e^{-z/L}), \tag{3}$$

where ν_0 is set around $35 \times 10^{-12}\,\mathrm{s\,m^{-2}}$, z is the height above the bottom boundary, and L is the chosen as 15 Mm. This form of frictional coefficient gives MF velocities a smooth transition to zero toward the bottom boundary $z = 0$.

Along with a special driver module, P. Vemareddy et al. (2024) first implemented the MF model in PENCIL CODE (Pencil Code Collaboration et al. 2021) and tested the evolution of a coronal magnetic field driven by observed photospheric magnetic fields. The PENCIL CODE is a highly modular physics-oriented simulation code that can be adapted to a wide range of applications. It is a finite-difference code using sixth order in space and third order in time differentiation schemes.

2.2. Initial Conditions

We use a potential field (PF) model (G. A. Gary 1989) as the initial field for the simulation. The PF is constructed from the normal component $(B_n \rightarrow B_z)$ of the observed vector magnetic field of the AR 11429 at 06:00 UT on 2012 March. As the PENCIL CODE operates on the vector potential ($\boldsymbol{A}$) rather than the magnetic field, the field divergence is satisfied without the need for extra schemes. The vector potential $\boldsymbol{A}_p$ of the PF is computed by imposing the Coulomb gauge condition ($\nabla \cdot \boldsymbol{A}_p = 0$) and has a vanishing normal component ($\boldsymbol{A}_p \cdot \hat{n} = 0$) at the bottom boundary (e.g., C. R. DeVore & S. K. Antiochos 2000). With these constraints, the components of $\boldsymbol{A}_p$ are computed as

$$A_{p,x}(x, y, z) = \mathrm{FT}^{-1}\left[\frac{ik_y}{k^2} \, \mathrm{FT}[B_z(x, y)] \, e^{-kz} \right] \tag{4}$$

$$A_{p,y}(x, y, z) = \mathrm{FT}^{-1}\left[\frac{-ik_x}{k^2} \, \mathrm{FT}[B_z(x, y)] \, e^{-kz} \right] \tag{5}$$

where k_x and k_y are wavevectors along the x and y directions, respectively, and $k = \sqrt{k_x^2 + k_y^2}$. Here, FT refers to the 2D Fourier transform operation on the observed $B_z(x, y)$ and FT^{-1} refers to the inverse Fourier transform. The observed B_z is

adjusted to satisfy the flux balance condition and is inserted in a larger area by padding the dimensions. The A_p is constructed on a uniform Cartesian computational grid of $192 \times 192 \times 120$ representing the AR coronal volume of physical dimensions $280 \times 280 \times 175 \, \text{Mm}^3$.

2.3. Time-dependent Boundary Conditions

In the data-driven MF models, the initial magnetic field at the start time of the simulation is driven by magnetic field observations of the photospheric boundary that represents the bottom of the computational domain (D. H. Mackay et al. 2011; S. L. Yardley et al. 2018). We obtained the ambiguity resolved HMI vector magnetic field components, which are served as an `hmi.sharp.cea_720s` data product in spherical coordinates. These are approximated to Cartesian components as $B_x \rightarrow B_\phi$, $B_y \rightarrow -B_\theta$, and $B_z \rightarrow B_r$ (M. G. Bobra et al. 2014) and are smoothed with a Gaussian width of 3 pixels both spatially and temporally. Also, the flux balance condition is applied to the B_z component. In order to reduce computation burden, the field components are rebinned by a factor of 4 such that each pixel corresponds to 2" on the computation grid. Driving the initial 3D field with photospheric magnetic fields leads to mild to moderate non-PFs, which may not represent the twisted core field of the ARs (S. L. Yardley et al. 2018). For complex ARs such as 11429, the observations have insufficient influx of magnetic energy and helicity, as a result the formation of low-lying twisted flux in the simulations has not been possible (P. Vemareddy et al. 2024). In this work, the initial field is driven by the electric fields ($E(x, y, z = 0, t)$), which are derived from time-sequence vector magnetic field observations of the AR (G. H. Fisher et al. 2010). The electric field has two components: an inductive field (E_I) and a non-inductive field component defined by the gradient of a scalar ψ

$$E = E_I - \nabla\psi \qquad (6)$$

The inductive component is obtained by solving the Faraday law of induction equation, $\partial_t B = -\nabla \times E_I$, which involves the poloidal-toroidal decomposition of the time derivative of the vector magnetic fields (G. H. Fisher et al. 2010). The non-inductive component requires a functional form for ψ, which is unknown and therefore invokes the following three different assumptions (M. C. M. Cheung & M. L. DeRosa 2012; M. C. M. Cheung et al. 2015):

$$\nabla^2\psi = 0 \qquad (7)$$

$$\nabla^2\psi = U(\nabla \times B)_z \qquad (8)$$

$$\nabla^2\psi = \Omega B_z \qquad (9)$$

where Ω and U are the free scalar parameters referring to the extent to which the axisymmetric vertical flux tube rotates and emerges, respectively. The first assumption is equivalent to zero contribution of non-inductive components, whereas the latter two cases are suggested by M. C. M. Cheung & M. L. DeRosa (2012) and M. C. M. Cheung et al. (2015) in order to ensure sufficient injection of magnetic helicity and free magnetic energy. The above chosen functional forms are linked to photospheric magnetic field observations and their horizontal spatial derivatives, and therefore the non-inductive part of E has horizontal components (x and y) that are being added to the inductive part of E. This form for non-inductive E has

vanishing horizontal divergence and as a result satisfies the induction equation such that $\partial B_z/\partial t = -\hat{z} \cdot (\nabla \times E_h)$ without modifying the B_z.

The derived photospheric electric fields at an interval of 12 minutes are being used as the driver field E at $z = 0$, instead of magnetic fields or vector potentials. At each instant of time, we add E at the bottom layer of the vector potential A in the computational domain and the time evolution of the magnetic field is determined by the time integration of the Faraday law

$$\frac{\partial A}{\partial t} = -E \qquad (10)$$

In the PENCIL CODE, we developed a driver module to read the time series of E at 12 minute intervals and interpolate them at the simulation time step.

The lateral sides of the simulation domain are specified with periodic boundary conditions and the top one is set to an open boundary condition.

3. Results

The AR 11429 was a successively erupting region during its disk passage (S. K. Dhakal et al. 2020; P. Vemareddy 2021). It produced three fast coronal mass ejections (CMEs) at an interval of about two days, which is a typical timescale for the buildup of magnetic energy by photospheric magnetic flux motions. As an example, the HMI observations of the photospheric vector magnetograms at two different times are displayed in Figures 1(a)–(b). The AR has a long polarity inversion line (PIL) in the northeast (NE) subregion between the P1 and N1 regions, in the southwest (SW) region between P2 and N2. These polarity regions exhibit shear motions, which can deform the magnetic field to align parallel to the local PIL. As a result, the horizontal vectors along the PIL are noticed to align parallel to the PIL as observed in the vector magnetograms. Both shear and converging motions are potential mechanisms to form a twisted magnetic flux at the core of the AR and then its further eruption (T. Amari et al. 2003). Similar to the successive erupting AR 12371 (P. Vemareddy 2017), S. K. Dhakal et al. (2020) suggested that the shearing motion and magnetic flux cancellation of opposite fluxes were the dominant factors to the recurrent homologous eruptions from this AR and are associated with the filament lying along the SW PIL. Under these observed conditions of the magnetic fluxes, after the first eruption on March 7 at 00:24 UT, this study is aimed at simulating the coronal field evolution until the next eruption on March 9 at 03:53 UT and then capturing the formation of the twisted FR that could erupt. To have a relaxed and approximate PF configuration after the first eruption, the simulation starting time is chosen to be 6:00 UT on March 7.

The time evolution of the derived magnetic parameters of vector magnetic field observations of the AR 11429 are plotted in Figures 1(c)–(e). The net flux ($\Phi_{N/S} = \sum_{\text{Pix}} Bz_{N/S} dA$, where dA is area of the pixel in the north (N) or south (S) polarity) exhibits decreasing evolution in time from 26×10^{21} to 24×10^{21} Mx in both polarities, which is presumed to be due to the converging motion of fluxes leading to their cancellations. From the time-sequence vector magnetic fields (B), the velocity field (V) is derived by a differential affine velocity estimator (DAVE4VM; P. W. Schuck 2008) and then we
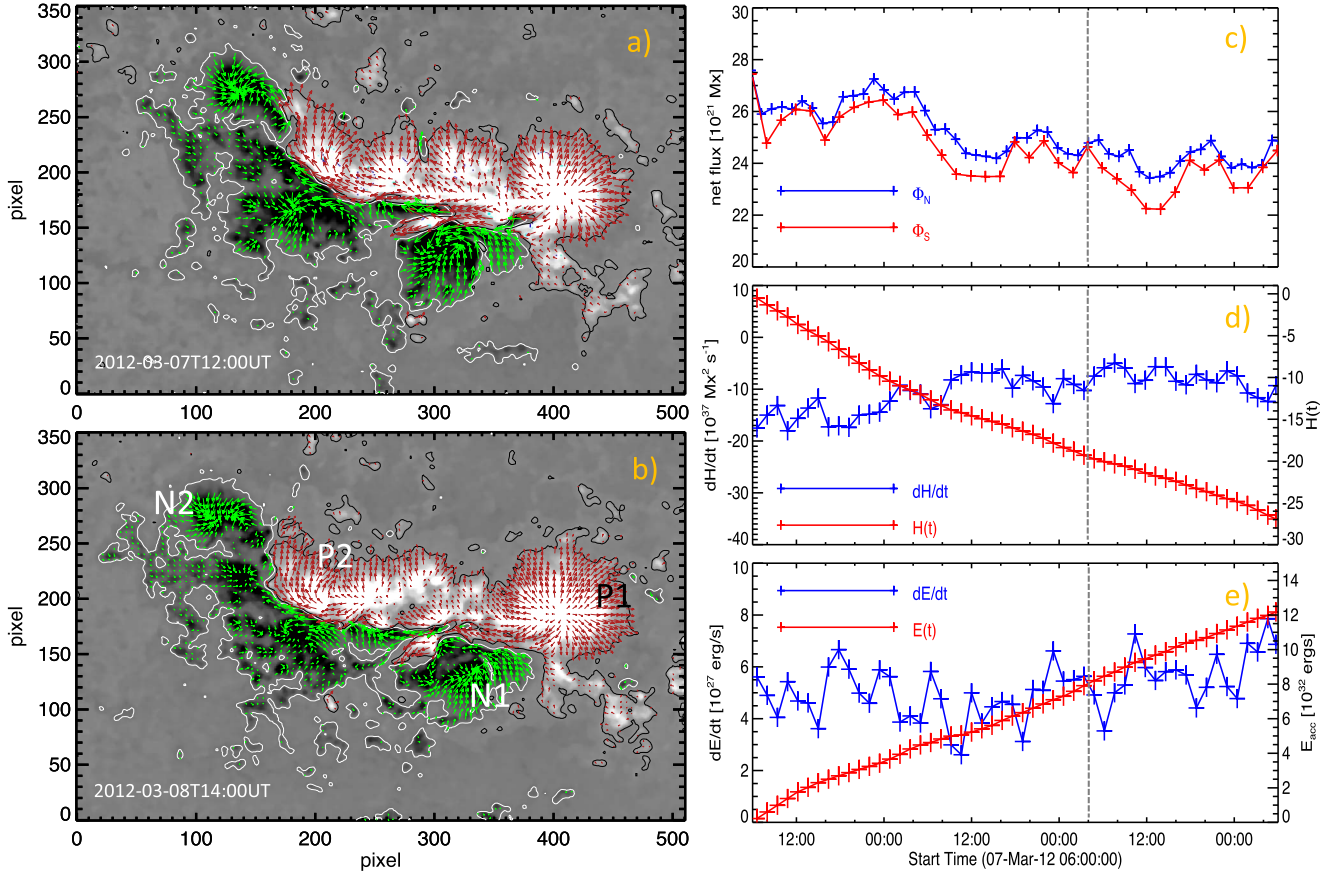
Figure 1. (a)–(b)) Vector magnetic field measurements of the AR 11429 at two different times in the evolution. Horizontal field vectors (arrows) are overplotted on the B_z map with labeled polarity regions. The axis units are in pixels of $0\overset{''}{.}5$. (c)–(e) Time evolution of net magnetic flux, helicity injection rate (dH/dt), and energy injection rate (dE/dt). The vertical dotted line refers to the eruption time at 03:44 UT on March 9.

compute the helicity injection rate through the photosphere as

$$\frac{dH}{dt}\bigg|_S = 2\int_S (\boldsymbol{A}_P \cdot \boldsymbol{B}_t)V_n dS - 2\int_S (\boldsymbol{A}_P \cdot \boldsymbol{V}_t)B_n dS \qquad (11)$$

where $\boldsymbol{A}_P$ is the vector potential of the PF $\boldsymbol{B}_p$, and the variables with subscripts n, t refer to normal and tangential components. The flux motions are injecting a net negative helicity at an average rate of $9 \times 10^{37}\,\mathrm{Mx}^2\,\mathrm{s}^{-1}$. At this rate, the corona has an accumulated net helicity of $20 \times 10^{42}\,\mathrm{Mx}^2$ over two days of evolution, which could be sufficient to launch a CME.

Similarly, the energy injection rate (Poynting flux) is calculated as

$$\frac{dE}{dt}\bigg|_S = \frac{1}{4\pi}\int_S B_t^2 V_n dS - \frac{1}{4\pi}\int_S (\boldsymbol{B}_t \cdot \boldsymbol{V}_t)B_n dS \qquad (12)$$

which is time integrated to evaluate the accumulated energy over a time period T as

$$E_{\mathrm{acc}} = \int_0^T \frac{dE}{dt}dt \qquad (13)$$

As can be noted from Figure 1(e), the observed energy injection leads to an accumulated energy of 8.4×10^{32} ergs, an energy budget for M-class flares.

3.1. Input Poynting Flux for Simulations

We drive the initial PF with the time-dependent electric field derived from the ad hoc assumptions given in Equations (7)–(9).

With the electric fields from the three assumptions, we perform essentially three simulation runs. The run R1 is based on the inductive electric field (E_I), whereas runs R2 and R3 include non-inductive contributions in order ensure sufficient injection of energy and helicity fluxes. For the latter two runs, one has to specify appropriate values for free parameters U and Ω. As suggested by J. Pomoell et al. (2019), these values are constrained by comparing the Poynting flux deduced from the DAVE4VM vector velocity and magnetic field (Figure 1(e) and Equation (9)) with that of the derived electric field ($dE/dt = \int \boldsymbol{E} \times \boldsymbol{B} \cdot d\boldsymbol{A}$) from these assumptions (J. Pomoell et al. 2019).

We use the values of $U = 120\,\mathrm{m\,s}^{-1}$ and $\Omega = 0.096\,\mathrm{turns\,day}^{-1}$ for R2 and R3, respectively. As shown in Figure 2, these values give a time-integrated Poynting flux of 18×10^{32} ergs until the eruption time (vertical dotted line), which is roughly a factor of 2 higher when compared with the observed one (Figure 1(e)). This difference is admitted for the following reasons: (i) the AR could be in a non-potential state even after the first eruption, (ii) the Poynting flux derived from DAVE4VM may be underestimated because the velocities represent averaged values over an apodising window typically $19 \times 19\,\mathrm{pixel}^2$, and (iii) the observational sensitivity of magnetic field measurements. With these existing difficulties, the chosen values of U and Ω are broadly constrained with an uncertainty of up to 40%. It should be noted that the coronal free energy is small (about 18 times), and the formation of the twisted flux is quite implausible with $\boldsymbol{E}_I$ alone, and therefore higher values of these free parameters are deemed necessary in
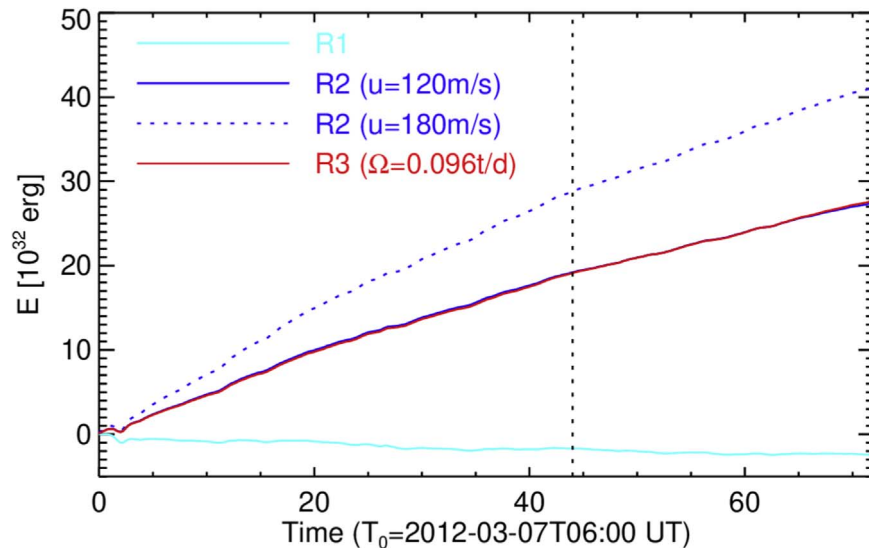
Figure 2. Time-integrated Poynting flux from the AR derived from the photospheric electric field. The run R1 is performed with an inductive electric field (E_I), whereas R2 and R3 are performed by electric fields, accounting for non-inductive contributions based on ad hoc assumptions, namely Equations (8) and (9). R2 is performed with $U = 120$ m s^{-1} and $U = 180$ m s^{-1}. The vertical dotted line refers to the eruption time at 03:44 UT on March 9.

order to pump sufficient free magnetic energy to generate magnetic structure that is comparable to observations.

3.2. Evolution of the Simulated Magnetic Structure

The abovesaid three types of MF simulations are performed by driving the initial PF with a time-dependent bottom boundary electric field for 72 hr duration starting from 6:00 UT on 2012 March 7 and for a further 24 hr without changing the lower boundary.

As explained earlier, the E field satisfies $\partial B_z / \partial t = -\hat{z} \cdot (\nabla \times E_h)$, reproducing the observed evolution of B_z self-consistently during the simulations. To check this, in Figure 3, we compare observed and simulated B_z at the $z = 0$ plane at 10 hr and 47 hr time instants of simulation R2. It can be noticed that the simulated B_z has a high degree of spatial correlation including small magnetic elements in the vicinity of sunspot regions. The scatter plots refer to a correlation of >99.95%, which implies the observed evolution of photospheric magnetic fields during the simulation. However, such a correlation is not true for horizontal components of B that are scaled by the free parameters in the non-inductive contribution of E in order to inject additional free energy and helicity.

Figure 4 presents the snapshots of the simulated magnetic structure of all three runs. Field lines are traced from the foot point locations where the horizontal magnetic field and total electric current are strong. From R1, one can see that the initial PF does not change significantly over several hours of evolution as the boundary electric field has inductive components derived from B_z components alone. In the runs R2 and R3, the initial magnetic structure evolved progressively to a highly twisted structure at the core of the AR surrounded by a less sheared field, which is evidently noticed in the snapshots at 25th hour. Further evolution until the 45th hour leads to transforming neighboring less sheared fields into twisted fields akin to a coherent FR along the PIL. Following this, the FR and the surrounding field grow and appear to rise in height, which is a typical signature of the initiation of the eruption. In the presence of magnetic diffusion and a supply of magnetic helicity through a time-dependent bottom boundary,

the MF relaxation method thus captures the formation and eruption of a magnetic flux rope in the AR. Using other codes, earlier studies (e.g., M. C. M. Cheung & M. L. DeRosa 2012; J. Pomoell et al. 2019) reported the simulated coronal field evolution capturing the FR formation in the emerging ARs.

It is worth pointing out that the electric fields in R2 are derived with the J_z distribution at the photosphere, and as a result one can expect a spatially varying twist about the PIL scaled by the free parameter U. And in R3 the non-inductive contributions to the derived electric fields are based on the B_z distribution scaled by the Ω; thus, the spatial variation of the magnetic twist along the PIL and its vicinity do not reflect the same observations as those of the electric fields in R2. Given this fact, the simulated 3D magnetic structure in R2 better reflects the coronal EUV observations than that in R3, as will be supported by the following comparative analysis with the observations.

The time evolution of the computed relative magnetic helicity (H) and magnetic energy in the simulated domain is plotted in Figure 5. In the MF relaxation of R1, the volume helicity (H) increases in magnitude from -4×10^{-9} to -0.37×10^{42} Mx^2. This is solely due to shear motions of fluxes along the PIL. Although there is no appreciable increase of total magnetic energy (E), the free magnetic energy ($E - E_p$) increases continuously, and it is 1.31×10^{32} ergs at the time of the eruption. During the simulation time of R1, the fractional free energy increases up to 10%.

That said, the H accumulates in the corona continuously (blue and red curves) and amounts to -39.2×10^{42} Mx^2 and -81.6×10^{42} Mx^2 for R2 and R3, respectively. Similarly, the total and free magnetic energies exhibit an increasing behavior as the coronal magnetic field becomes twisted. In these runs, the fractional free energy corresponds to 47% (R2) and 57% (R3) at the time of the eruption, which is probably significant enough to initiate the rise motion of the FR. Numerical simulations by T. Amari et al. (2003) reported a fractional free energy of 5% to initiate the eruption, while TMF simulations by J. Pomoell et al. (2019) refer to 14%–50% of fractional free energy that resulted in an erupting FR; therefore, our results are more aligned with latter ones as the simulation setup is the
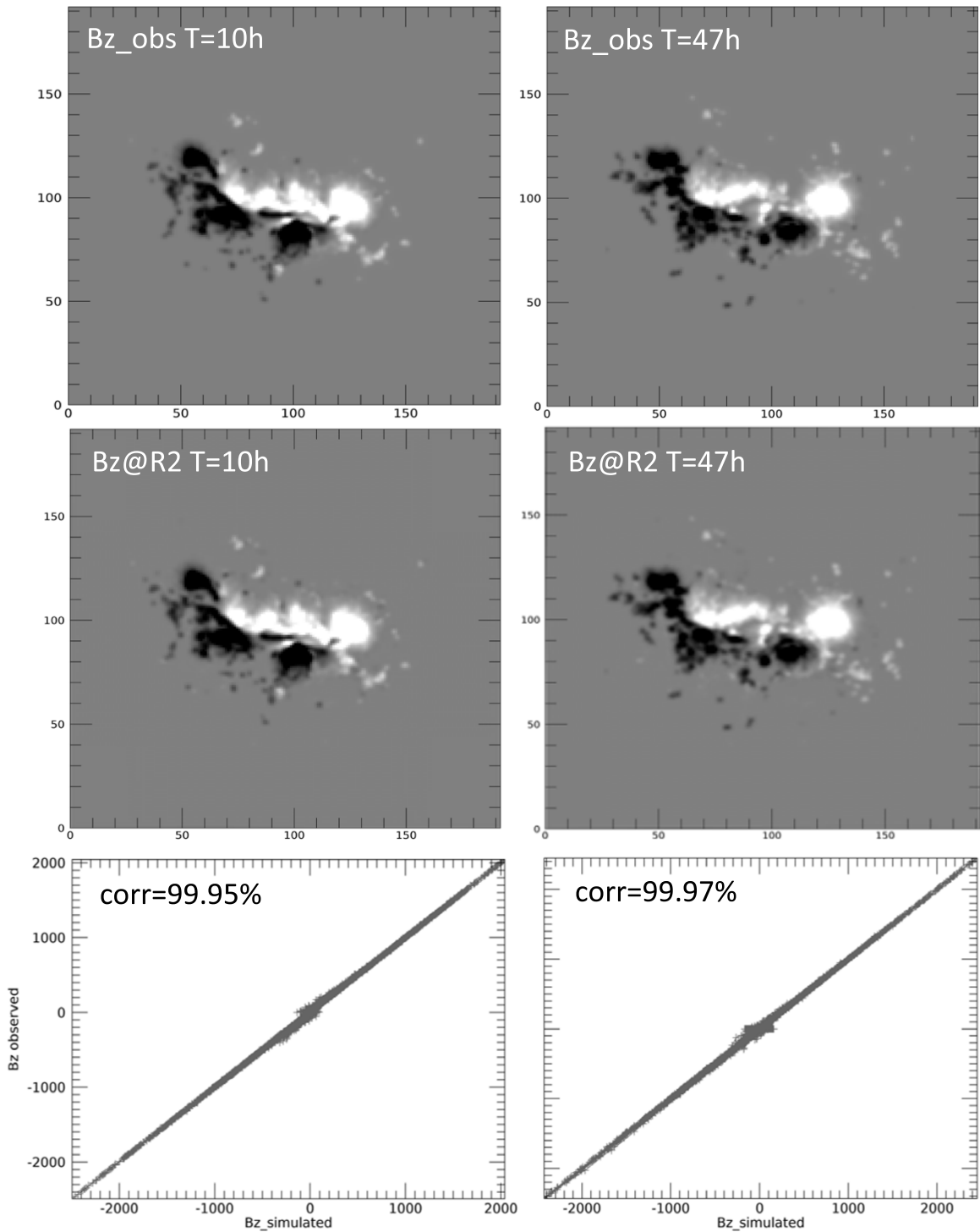
Figure 3. Reproducibility of observed B_z at the photosphere with the MF simulation driven by the E field. Top row: observed B_z at 10 hr and 47 hr from the start of the simulation (i.e., 2012-03-07T06:00 UT). Middle row: $B_z|_{z=0}$ of R2 at 10 hr and 47 hr, which have a one-to-one spatial correlation with the observations. Note that these maps are scaled with ±900 G. Bottom row: scatter plots of observed and simulated B_z showing a correlation of 99.95%.

same. It is important to note that the coronal estimates of helicity (H) for R3 is higher by a factor of 2 than that for R2, even though the same amounts of energy fluxes are injected for these runs. As discussed earlier, the higher value of H is due to the uniform distribution of the twist nature arising from Equation (8); correspondingly, the coronal field is highly twisted in R3.

3.3. Comparing the Simulated Magnetic Structure with Coronal Observations

We performed another simulation of R2 driven by electric fields with free parameter $U = 180\,\mathrm{m\,s^{-1}}$. This run is to understand the FR formation timescale and rise motion during a given time evolution. From the comparison, the twisted flux formation in this run happened early, and later its rise motion
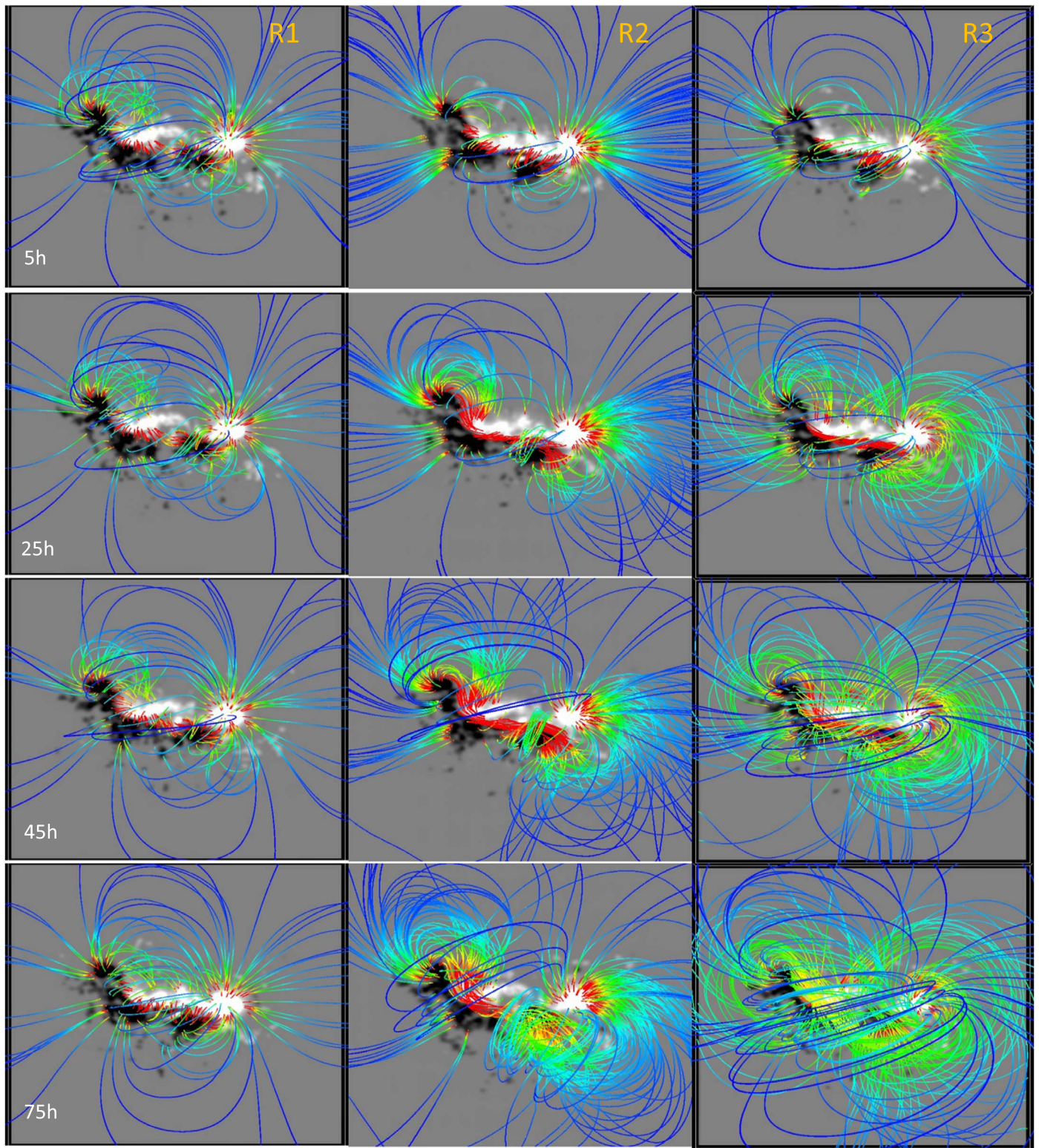
Figure 4. Snapshots of magnetic structure at different epochs of the simulation: R1 (first column), R2 (second column), and R3 (third column). Magnetic field lines are colored by their field strengths and the background image is the normal magnetic field B_z at the bottom of the computational domain ($z = 0$). In R2 and R3, the magnetic field evolution captures the formation of the twisted flux rope along the PIL. The image sequence of all three simulation runs at 1 hr intervals is attached as an animation.

(An animation of this figure is available in the online article.)

reached higher heights. Figure 6(a) displays the rendered magnetic structure of R2 ($U = 180 \, \mathrm{m \, s^{-1}}$) with B_z as the background image. The modeled magnetic structure consists of

a low-lying, twisted core field along the PIL overlaid by potential arcades and J-shaped field lines (lobes or elbow field lines) sheared past each other in the SW and NE regions, which
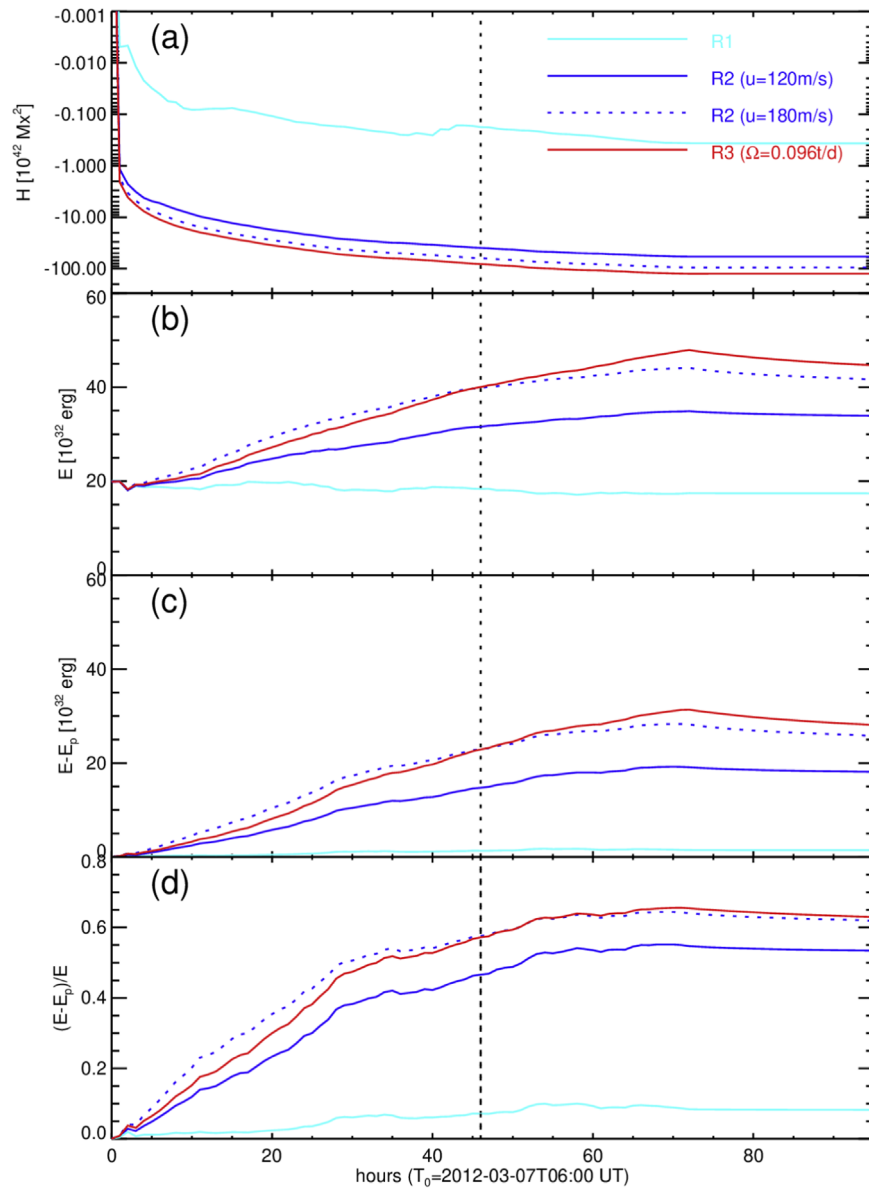
Figure 5. Time evolution of energy and helicity parameters in the computational domain. (a) Total magnetic helicity, (b) total magnetic energy, (c) free magnetic energy, and (d) fractional free energy with respect to the total energy. Cyan, blue, and red color curves refer to runs R1, R2, and R3, respectively. The vertical dotted line refers to the eruption time at 03:44 UT on March 9, at which time the free-energy fraction is 7%, 47%, and 57% for R1, R2, and R3, respectively.

together manifest an inverse S-sigmoidal structure. Although the global AR magnetic configuration is inverse S-shaped, the magnetic field in the SW region alone mimics another inverse S sigmoid. As shown in Figure 6(b)–(c), the magnetic structure qualitatively resembles the morphology of coronal features captured in Atmospheric Imaging Assembly (AIA) images. Owing to high temperatures, sigmoids are often seen in hot EUV channels. The AIA 335 Å image ($T \approx 2.5$ MK) displays a coronal sigmoid resembling the simulated magnetic structure and plasma loops trace the magnetic field in the AIA 171 Å snapshot. The AIA 304 Å wave band is a cool channel ($T \approx 5 \times 10^4$ K) image exhibiting a filament channel in the SW region, which is plasma embedded in the dips of the twisted field of the sigmoid configuration.

The simulated magnetic structure is rendered in perspective, as depicted in Figure 7 at different times. The initial PF becomes sheared, progressively forming inverse J-shaped field lines surrounding the low-lying twisted core field along the

PIL. In a timescale of two days, a well-developed twisted flux builds up along the PIL. Thereafter the twisted magnetic structure ascends in height with time, especially the field in the SW region, from 40 to 120 Mm (see the attached animation). This rise motion corroborates the observations of the eruption from the SW region of the AR (S. K. Dhakal et al. 2020). We emphasize that the rise motion does not turn into an eventual eruption like the observed onset of eruptions; rather, it is progressive in time, even after driving stopped at 72 hr. Since the velocity is controlled by the ν parameter, the TMF simulations implicitly lacks the short-term dynamic evolution, although they capture the buildup of free magnetic energy during the slow evolution over long times.

Since the MF model does not include the thermodynamic evolution of the plasma, we cannot synthesize images of coronal emission in EUV or X-ray wavelengths. To produce synthetic maps of coronal loops similar to EUV images, M. C. M. Cheung & M. L. DeRosa (2012) introduced a method
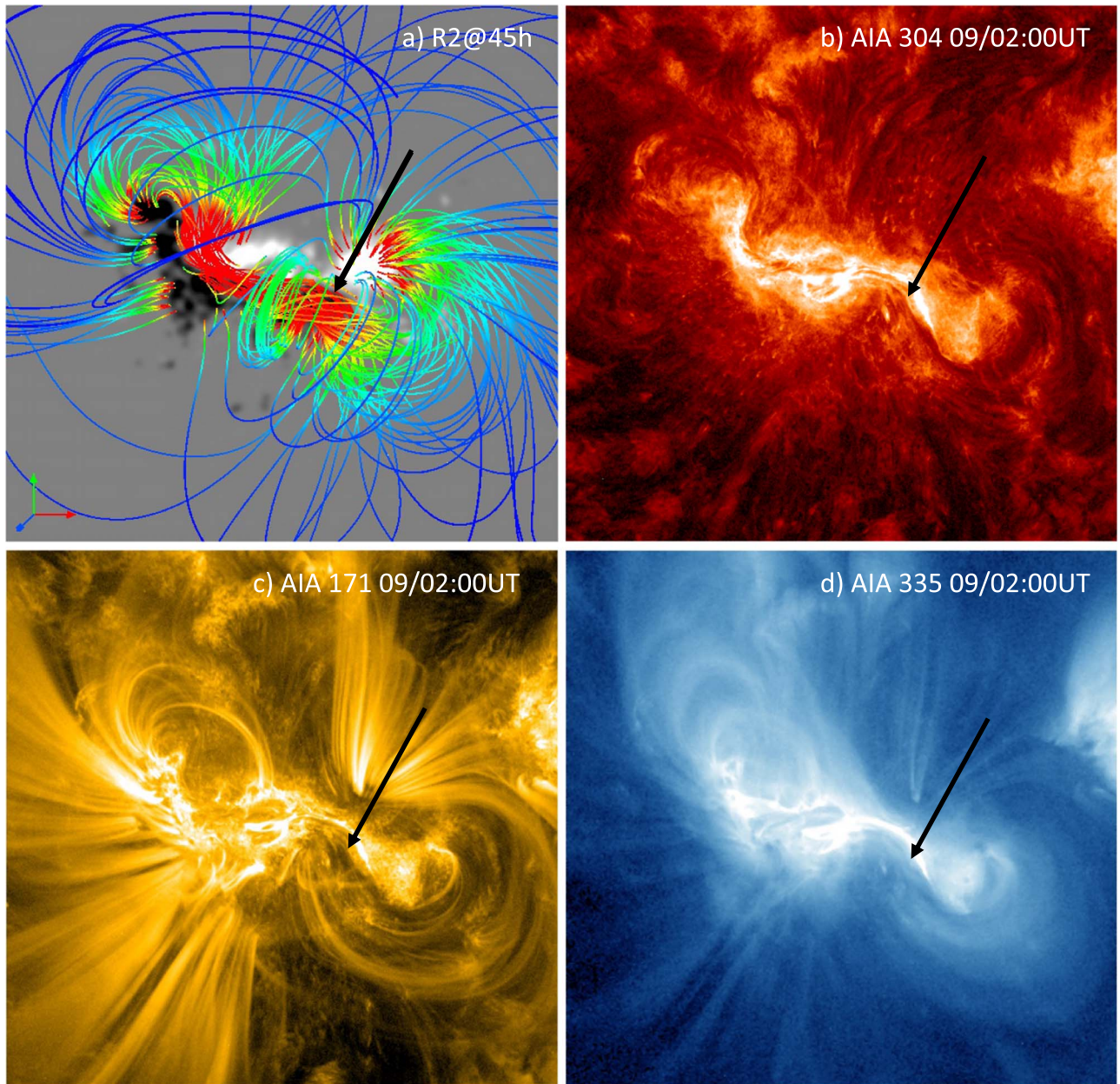
Figure 6. Comparison of pre-eruptive magnetic structure of R2 ($U = 180$ m s^{-1}) with the coronal plasma tracers in AIA images of the AR 11429. (a) Top view of rendered magnetic structure at the 45th hour of simulation R2. The background image is the B_z distribution at $z = 0$. (b)–(d) AIA 304, 171, and 335 Å images at 2:00UT on March 9. The morphology in these images depicts the structured corona of the twisted flux rope that resembles the simulated magnetic field. The black arrow points to the eruptive filament manifested by the twisted field in SW region.

to generate proxy emissivities based on the modeled magnetic field alone. Proxy emissivities are derived with the values of square of the total current density (J^2) averaged along a magnetic field line. This technique is useful for a qualitative visualization of coronal loops in a magnetic model such as MF; however, it is not a replacement for more sophisticated techniques that use the thermodynamic variables from MHD models (e.g., R. Lionello et al. 2009; V. H. Hansteen et al. 2010). Following their method, we computed the emissivity ($\varepsilon(x, y, z)$) at each grid point in the computational domain. This volume distribution of emissivity is integrated in the vertical direction to generate a 2D distribution, as seen in coronal EUV observations. Such proxy emission maps at two epochs are compared with the respective AIA 304 and 335 Å images in Figure 8. We can notice a striking morphological similarity of

the modeled emission with the diffuse plasma emission of the sigmoid captured in the 335 Å image and a trace of the dark filament present in the 304 Å image. This filament is regarded as an FR in the models, and it is expanding and rising in time as observed in the vertical cross-section planes.

3.4. Topological Analysis of Simulated Magnetic Structure

For a topological study, we analyze the quasi-separatrix layers (QSLs; V. S. Titov et al. 2002) where the magnetic field line linkage changes drastically in the volume. The strength of QSLs is measured by squashing factor Q. From the simulated magnetic structure, we computed Q with the procedures of R. Liu et al. (2016), and its map is displayed in Figure 9(a). In this map, QSLs with large Q values ($>10^6$) are identified by
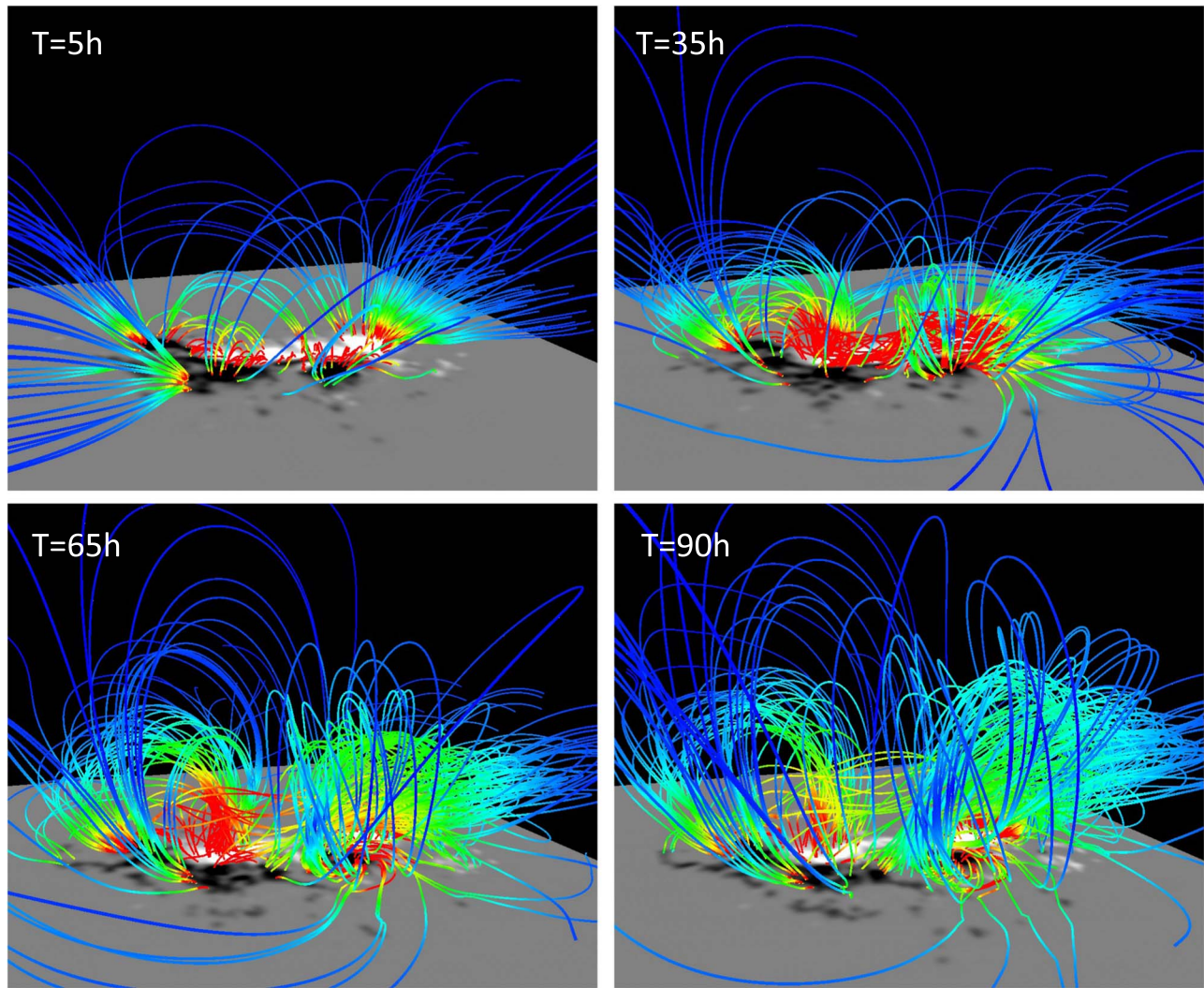
Figure 7. Perspective view of the rendered magnetic structure of R2 at 5, 35, 65, and 90 hr, respectively. From the initial potential field, the structure evolves to sheared field consisting of inverse J-shaped field lines surrounding the low-lying twisted core field along the PIL. In a timescale of two days, a well-developed twisted flux rope forms, which then runs into slow explosive stage in the corona. In order to comprehend the simulated evolution of this run, the image sequence of 96 hr duration at 1 hr intervals is attached as an animation. Note that the filament embedded twisted structure in the SW region rises in height progressively.
(An animation of this figure is available in the online article.)

intense white traces in strong field regions. A continuous trace of Q can be noticed along the main PIL.

To compare QSL locations with the flare ribbon emission, the AIA 1600 Å, 304 Å, and 131 Å observations during the impulsive phase of the flare are displayed in the panels of Figures 9(b)–(d), respectively. On these images, contours of Q at 10^5 and 10^6 levels are overplotted by removing the irrelevant QSLs with a mask on the Q map. The ribbon emission is related to the erupting MFR in the SW region, which is cospatial with the QSL section of the simulated magnetic configuration. Unlike the QSLs determined in the NLFFF models (P. Vemareddy 2021), the QSLs in this simulation better represent the twisted core flux along the PIL and the observed ribbon emission.

From the theoretical studies, it was predicted that the flare ribbons are the photospheric/chromospheric footprints of QSLs that enclose a twisted FR (P. Demoulin et al. 1996). The extremities of the ribbons are found to be hook shaped for weakly twisted FRs and are spiral shaped for highly twisted

FRs (J. Zhao et al. 2016). The observed ribbon morphology in our case delineates an inverse S shape with cospatial hooks in the extreme ends; therefore, the enclosed FR is indicated to be moderately twisted. This finding is consistent with previously reported pre-eruptive NLFFF configurations (M. G. Bobra et al. 2008; Y. Su & A. van Ballegooijen 2013; R. Liu et al. 2016; P. Vemareddy 2021). In Figure 10, we display Q and twist number (tw) maps computed from the vertical cross section of the erupting FR at three different times. In these maps, the QSLs of large Q values well distinguish two closed domains belonging to twisted core sections above the PIL and the surrounding less sheared arcade. With the twisted flux (flux rope) at the core, the QSLs in the cross section resemble an inverse tear-drop shape as evidenced by the theoretical/ numerical models (C. Jiang et al. 2018; P. Vemareddy 2019). The twist of the field lines at the core is negative; therefore, field lines are left helical and the FR has an inverse S morphology. Within the FR cross section, the total twist of the field lines varies in the range of two turns; however, the
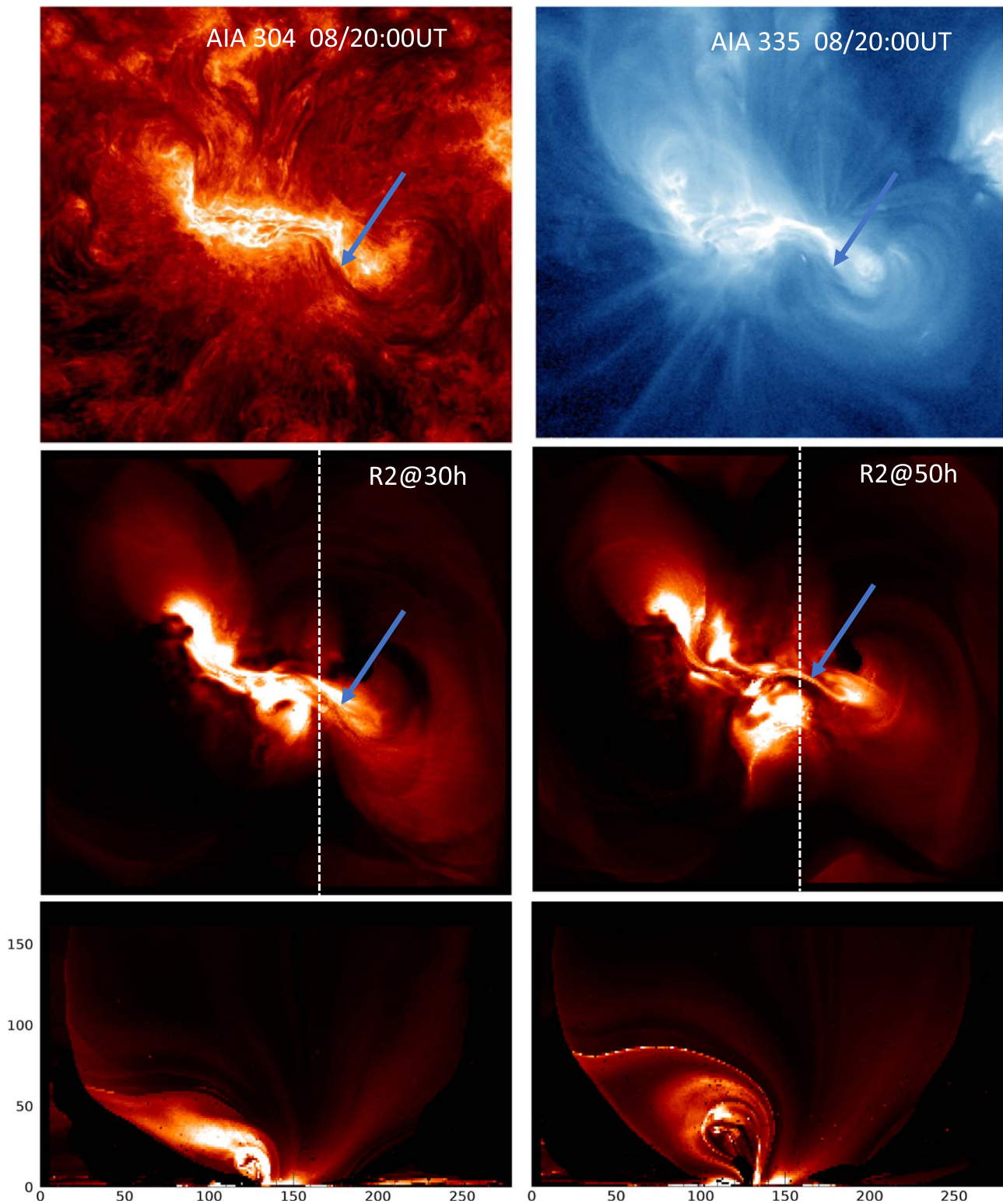
Figure 8. Comparison of proxy emission maps with the coronal EUV images. Top row: AIA 304 Å and 335 Å observations of the AR 11429. Middle row: proxy emission maps synthesized from the simulated magnetic field of R2 at the time instances of 30 hr and 50 hr. A visual inspection of these maps suggests that the spatial features presented in the AIA 304 and 335 Å images have a striking morphological similarity, especially a low-lying filament feature (pointed at by the arrow) and high-lying coronal sigmoidal loops. The white dashed line refers to the position of the vertical slice plane. Bottom row: proxy emission in the vertical slice plane captures the twisted flux rope and its upward motion in time. Axes units are in Mm.

average twist number is well below one turn, so that the twisted flux is in stable equilibrium. After the formation in the first few hours, the twisted FR expands and rises up in time, as delineated in Figure 10.

4. Summary and Discussion

In this study, the evolution of the magnetic structure of AR 11429 is simulated by a time-dependent MF model. The computational procedure is implemented in the PENCIL code,
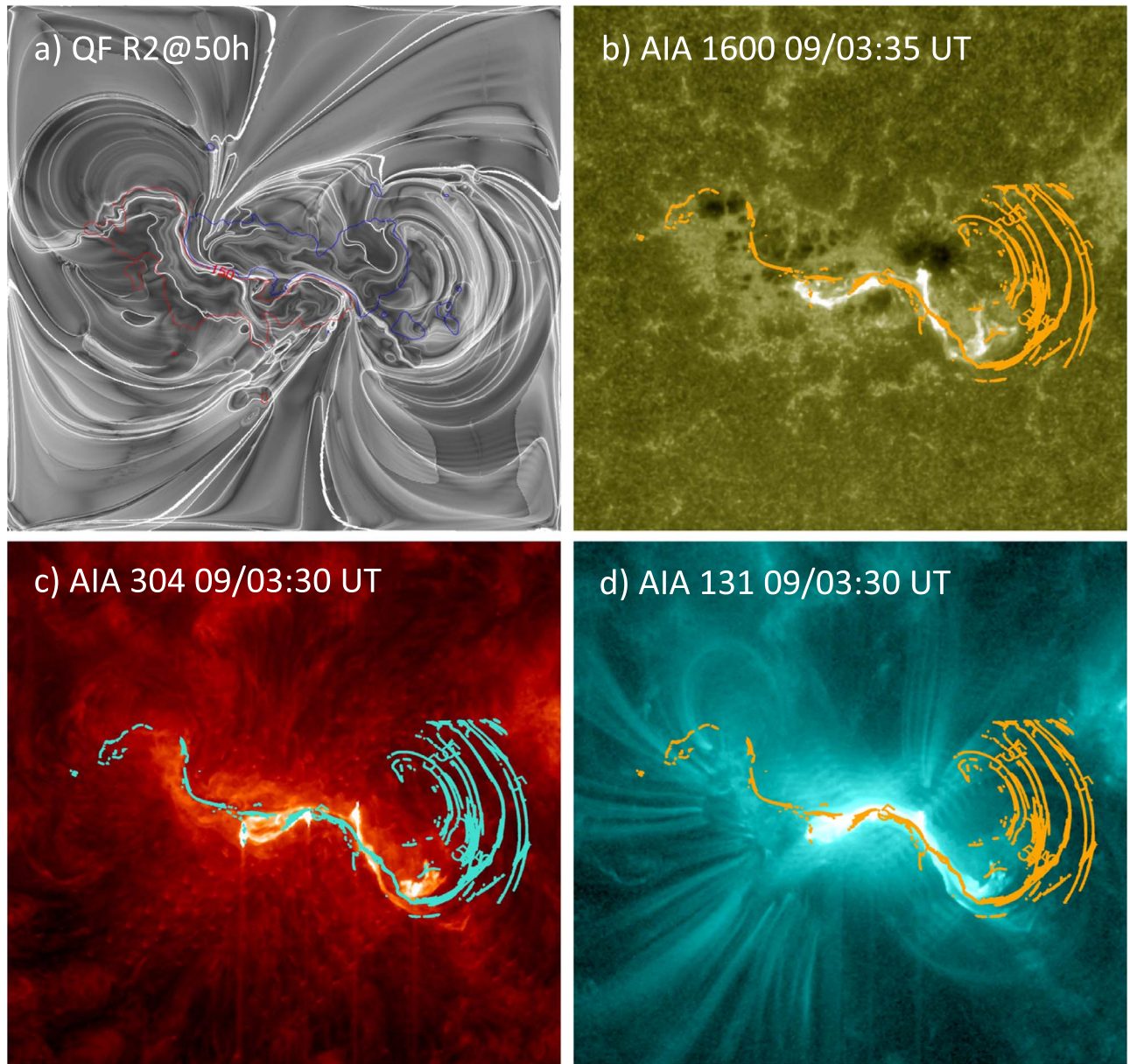
Figure 9. Comparison of QSLs with flare ribbons. (a) Log(Q) map at $z = 1.45$ Mm computed from the magnetic structure of R2 at the 50 hr time instant. Contours of B_z at ± 150 G are overdrawn (red/blue curves), and QSLs with large Q values are identified by intense white traces in the strong field region. (b)–(d) AIA 1600, 304, and 131 Å images overlaid with contours of $\ln(Q) = [5, 6]$ (in cyan/orange color). Irrelevant QSLs are removed by applying a mask on the Q map. Note the intense flare ribbon emission underneath the erupting flux rope is cospatial with the QSL section in the SW subregion.

which is based on a uniform grid. Invoking ad hoc assumptions, the non-inductive electric fields are derived from time-sequence vector magnetic field observations of the AR obtained by HMI and supplement inductive components in order to inject sufficient free magnetic energy from the bottom of the computational domain, as suggested by M. C. M. Cheung & M. L. DeRosa (2012). Unlike staggered grid based MHD codes (K. Hayashi et al. 2019; J. Pomoell et al. 2019), in our implementation the electric fields are defined at the bottom boundary, where magnetic fields are defined, too, and the vertical component of the photospheric magnetic field is reproduced accurately through the induction equation (see Figure 3).

The simulated magnetic structure evolves from a potential to twisted fields over the course of two days, depicting the formation of an FR and its eventual eruption as a large-scale CME. While the ARs have a nonuniform field line twist distribution in and around the PIL, the simulated magnetic structure of R2 (driven by an electric field based on the U assumption) is better comparable with the observed coronal morphology than R3 (driven by electric fields based on the Ω assumption). The magnetic configuration is an inverse S-sigmoidal structure, composed of a PF enveloping the inverse J-shaped fields that are sheared past one another and a low-lying twisted field along the major PIL. Proxy emission maps are generated from the simulated field and compared with the observations. These emission maps exhibit a remarkable one-to-one correspondence with the spatial characteristics in the 304 and 335 Å wave band coronal pictures (Figure 8), particularly the filament channel that is being erupted from the SW region (S. K. Dhakal et al. 2020). We further conducted a topological analysis of simulated fields to understand the
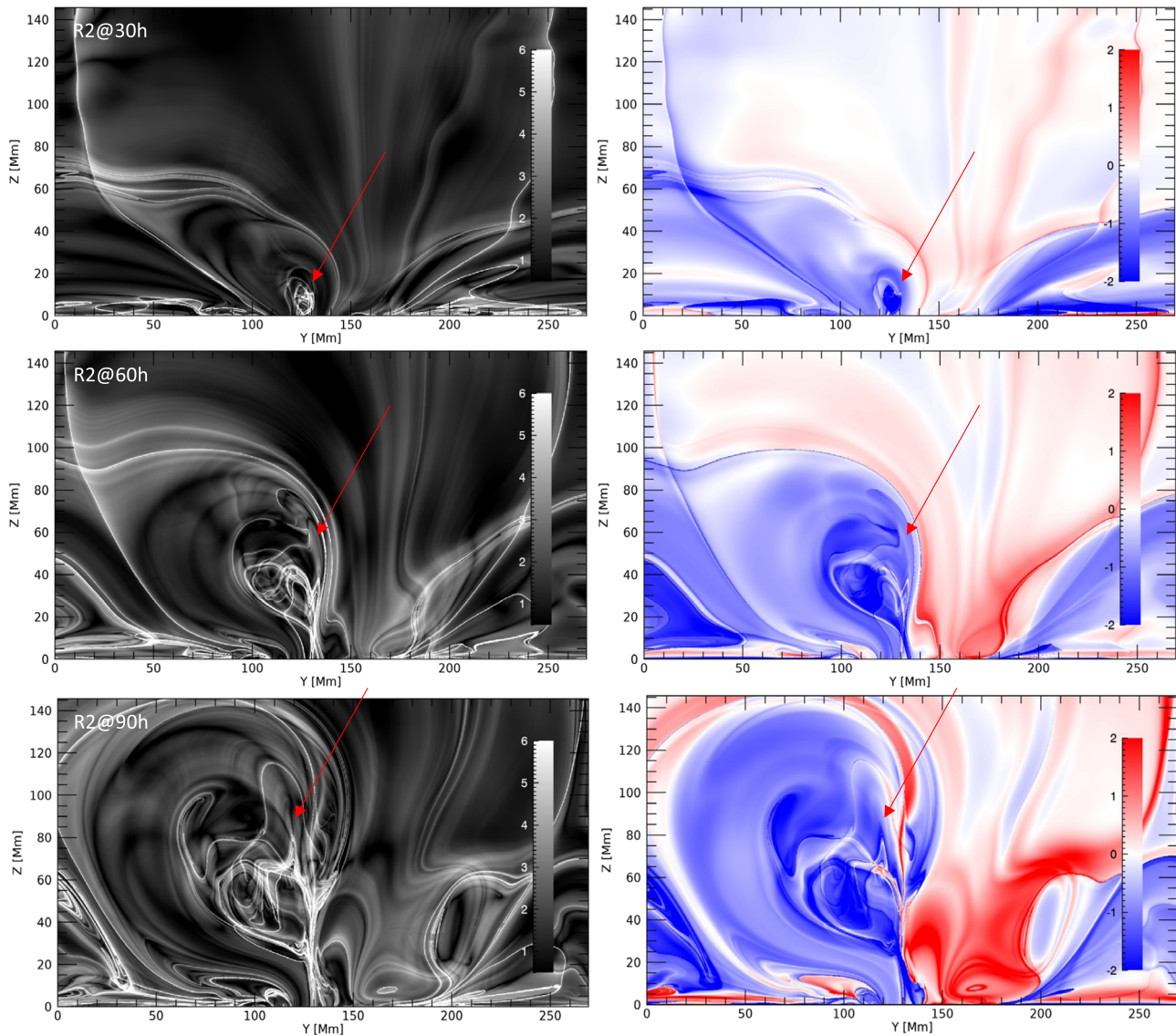
Figure 10. ln(Q) and twist distribution in the vertical slice placed across the rising flux rope as shown in Figure 8. Left column: maps of ln(Q) at three different times of R2. QSLs of large Q values (white) are boundaries of magnetic domains enclosing the twisted flux (red arrows) about the PIL. Right column: twist distribution at three different times. Twist values refer to left-handed helicity of field lines in the flux rope. Note the upward rise motion of the flux rope in time (top to bottom).

validity of the modeled twisted FR. The QSLs are distributed cospatially with the observed flare ribbons, consistent with the standard flare models; therefore, the extent of the twist and orientation of the erupting FR are indicated to be consistent with the real scenario in this case.

Employing the TMF model, we simulate the long-term coronal field evolution, correctly capturing the formation of the twisted FR mimicking a coronal sigmoid and then its eruption as seen in the AR. These simulations are very useful to shed light on the mechanisms responsible for the CME eruptions in the source ARs. One drawback of these simulations is that the erupting phase of the FR is not eventual such as in the observed solar cases. The eruption phase is slow as the simulation proceeds in time (see the animation associated with Figure 7) after the twisted FR formed, which is an inherent property of the MF model because the velocity is controlled by the frictional parameter. Under these circumstances, one can use the twisted field generated from these TMF simulations as the initial condition for the full MHD or data-inspired simulations (e.g., C. Jiang et al. 2018; S. Inoue et al. 2023) to reproduce the

actual eruption scenario, which will be focused on in our future investigations.

ORCID iDs

P. Vemareddy ● https://orcid.org/0000-0003-4433-8823

References

Amari, T., Luciani, J. F., Aly, J. J., et al. 2003, ApJ, 585, 1073
Bobra, M. G., Sun, X., Hoeksema, J. T., et al. 2014, SoPh, 289, 3549

Bobra, M. G., van Ballegooijen, A. A., & DeLuca, E. E. 2008, ApJ, 672, 1209
Cheung, M. C. M., De Pontieu, B., Tarbell, T. D., et al. 2015, ApJ, 801, 83
Cheung, M. C. M., & DeRosa, M. L. 2012, ApJ, 757, 147
DeRosa, M. L., Schrijver, C. J., Barnes, G., et al. 2009, ApJ, 696, 1780
Demoulin, P., Henoux, J. C., Priest, E. R., & Mandrini, C. H. 1996, A&A, 308, 643
DeVore, C. R., & Antiochos, S. K. 2000, ApJ, 539, 954
Dhakal, S. K., Zhang, J., Vemareddy, P., & Karna, N. 2020, ApJ, 901, 40
Fisher, G. H., Welsch, B. T., Abbett, W. P., & Bercik, D. J. 2010, ApJ, 715, 242
Gary, G. A. 1989, ApJS, 69, 323
Gibb, G. P. S., Mackay, D. H., Green, L. M., & Meyer, K. A. 2014, ApJ, 782, 71
Gibson, S. E., Kucera, T. A., White, S. M., et al. 2016, FrASS, 3, 8
Gudiksen, B. V., & Nordlund, Å. 2002, ApJL, 572, L113
Hansteen, V. H., Hara, H., De Pontieu, B., & Carlsson, M. 2010, ApJ, 718, 1070
Harvey, J. W., Hill, F., Hubbard, R. P., et al. 1996, Sci, 272, 1284
Hayashi, K., Feng, X., Xiong, M., & Jiang, C. 2019, ApJL, 871, L28
Inoue, S. 2016, PEPS, 3, 19
Inoue, S., Hayashi, K., & Miyoshi, T. 2023, ApJ, 946, 46
Jiang, C., Feng, X., Guo, Y., & Hu, Q. 2022, Innov, 3, 100236
Jiang, C., Zou, P., Feng, X., et al. 2018, ApJ, 869, 13
Keller, C. U., Harvey, J. W., & Giampapa, M. S. 2003, Proc. SPIE, 4853, 194
Landi, E., Hutton, R., Brage, T., & Li, W. 2020, ApJ, 904, 87
Lin, H., Kuhn, J. R., & Coulter, R. 2004, ApJL, 613, L177
Lionello, R., Linker, J. A., & Mikić, Z. 2009, ApJ, 690, 902
Liu, R., Kliem, B., Titov, V. S., et al. 2016, ApJ, 818, 148
Mackay, D. H., Green, L. M., & van Ballegooijen, A. 2011, ApJ, 729, 97
Masson, S., Pariat, E., Aulanier, G., & Schrijver, C. J. 2009, ApJ, 700, 559
Mikić, Z., Linker, J. A., Schnack, D. D., Lionello, R., & Tarditi, A. 1999, PhPl, 6, 2217
Pencil Code Collaboration, Brandenburg, A., Johansen, A., et al. 2021, JOSS, 6, 2807
Pomoell, J., Lumme, E., & Kilpua, E. 2019, SoPh, 294, 41
Raouafi, N. E., Riley, P., Gibson, S., Fineschi, S., & Solanki, S. K. 2016, FrASS, 3, 20
Régnier, S. 2013, SoPh, 288, 481
Régnier, S., & Amari, T. 2004, A&A, 425, 345
Sakurai, T. 1989, SSRv, 51, 11
Scherrer, P. H., Bogart, R. S., Bush, R. I., et al. 1995, SoPh, 162, 129
Scherrer, P. H., Schou, J., Bush, R. I., et al. 2012, SoPh, 275, 207
Schou, J., Scherrer, P. H., Bush, R. I., Wachter, R., et al. 2012, SoPh, 275, 229
Schrijver, C. J., DeRosa, M. L., Metcalf, T., et al. 2008, ApJ, 675, 1637
Schuck, P. W. 2008, ApJ, 683, 1134
Shibata, K., & Magara, T. 2011, LRSP, 8, 6
Si, R., Brage, T., Li, W., et al. 2020, ApJL, 898, L34
Su, Y., & van Ballegooijen, A. 2013, ApJ, 764, 91
Titov, V. S., Hornig, G., & Démoulin, P. 2002, JGRA, 107, 1164
Tomczyk, S., Card, G. L., Darnell, T., et al. 2008, SoPh, 247, 411
Toriumi, S., Takasao, S., Cheung, M. C. M., et al. 2020, ApJ, 890, 103
Valori, G., Kliem, B., & Keppens, R. 2005, A&A, 433, 335
van Ballegooijen, A. A., Priest, E. R., & Mackay, D. H. 2000, ApJ, 539, 983
Vemareddy, P. 2017, ApJ, 845, 59
Vemareddy, P. 2019, ApJ, 872, 182
Vemareddy, P. 2021, FrP, 9, 605
Vemareddy, P., & Demóulin, P. 2018, ApJ, 857, 90
Vemareddy, P., Warnecke, J., & Bourdin, P. A. 2024, RAA, 24, 025007
Vemareddy, P., & Wiegelmann, T. 2014, ApJ, 792, 40
Wiegelmann, T., Petrie, G. J. D., & Riley, P. 2017, SSRv, 210, 249
Yang, W. H., Sturrock, P. A., & Antiochos, S. K. 1986, ApJ, 309, 383
Yardley, S. L., Mackay, D. H., & Green, L. M. 2018, ApJ, 852, 82
Zhao, J., Gilchrist, S. A., Aulanier, G., et al. 2016, ApJ, 823, 62